Anuário do Instituto de Geociências
Universidade Federal do Rio de Janeiro
https://revistas.ufrj.br/index.php/aigeo/

ISSN 0101-9759
e-ISSN 1982-3908

GEOLOGY

Fire-Induced Thermal Alteration in Iron Meteorites: Metallographic Analysis of the 2018 Disaster at the National Museum of Rio de Janeiro

Alteração Térmica Induzida por Fogo em Meteoritos de Ferro: Análise Metalográfica do Desastre no Museu Nacional do Rio de Janeiro de 2018

Felipe Abrahão Monteiro[1], Maria Elizabeth Zucolotto[2], Amanda Araujo Tosi[1]

[1]Universidade Federal do Rio de Janeiro, Instituto de Geociências, Departamento de Geologia, Rio de Janeiro, RJ, Brasil
[2]Universidade Federal do Rio de Janeiro, Museu Nacional, Departamento de Geologia e Paleontologia, Setor de Meteoritos, Rio de Janeiro, RJ, Brasil
E-mails: famont10@gmail.com; meteoritos@mn.ufrj.br; amandatosi@hotmail.com

Abstract

The fire that destroyed the main building of the National Museum of Rio de Janeiro (MN/UFRJ) on 2 September 2018 exposed one of the largest meteorite collections in the Southern Hemisphere to highly heterogeneous thermal conditions. Iron meteorites stored in different sectors of the building experienced markedly variable thermal stress, ranging from negligible heating to intense reheating beneath collapsed, thermally insulating debris. This study presents a detailed metallographic investigation of iron meteorites from the MN/UFRJ collection, aimed at identifying and characterizing fire-induced thermal alterations, distinguishing them from primary meteoritic features, and establishing a practical framework for damage documentation and classification. Comparative optical microscopy, SEM–EDS analyses, and Ni–P chemical profiling reveal a continuous sequence of diffusion-driven microstructural modifications, including attenuation or loss of Neumann bands, recrystallization and fragmentation of kamacite, redistribution of Ni and P at metal interfaces, and partial destabilization of schreibersite. Based on these systematic patterns, a seven-level thermal damage classification (F0–F7) is proposed, correlating observable metallographic features with inferred temperature–time conditions, from pristine Widmanstätten structures to complete melting and resolidification of the metallic mass. The classification scheme is applied to the MN/UFRJ collection and incorporated into specimen records and physical labels, supporting both scientific interpretation and conservation planning. More broadly, the results demonstrate that even short-lived fire exposure can imprint diagnostic and quantifiable overprints on meteoritic microstructures, underscoring the necessity of recognizing and documenting anthropogenic thermal alteration when studying and preserving meteorite collections worldwide.

Keywords: Fe–Ni alloys; Widmanstätten pattern; Thermal damage classification

Resumo

O incêndio que destruiu o prédio principal do Museu Nacional do Rio de Janeiro (MN/UFRJ) em 2 de setembro de 2018 expôs uma das maiores coleções de meteoritos do Hemisfério Sul a condições térmicas altamente heterogêneas. Meteoritos de ferro armazenados em diferentes setores do prédio sofreram estresse térmico marcadamente variável, desde aquecimento insignificante até intenso reaquecimento sob escombros colapsados e termicamente isolantes. Este estudo apresenta uma investigação metalográfica detalhada de meteoritos de ferro da coleção do MN/UFRJ, com o objetivo de identificar e caracterizar as alterações térmicas induzidas pelo fogo, distinguindo-as das características primárias dos meteoritos e estabelecendo um arcabouço prático para documentação e classificação de danos. Microscopia óptica comparativa, análises SEM-EDS e perfil químico Ni-P revelam uma sequência contínua de modificações microestruturais impulsionadas por difusão, incluindo atenuação ou perda de bandas de Neumann, recristalização e fragmentação da kamacita, redistribuição de Ni e P nas interfaces metálicas e desestabilização parcial da schreibersita. Com base nesses padrões sistemáticos, propõe-se uma classificação de danos térmicos em sete níveis (F0–F7), correlacionando características metalográficas observáveis com condições inferidas de temperatura e tempo, desde estruturas de Widmanstätten intactas até a fusão completa e resolidificação da massa metálica. O esquema de classificação é aplicado à coleção do MN/UFRJ e incorporado aos registros de

Received: December 18, 2025; Accepted: January 8, 2026

espécimes e etiquetas físicas, auxiliando tanto a interpretação científica quanto o planejamento de conservação. De forma mais ampla, os resultados demonstram que mesmo uma breve exposição ao fogo pode imprimir sobreposições diagnósticas e quantificáveis nas microestruturas meteoríticas, ressaltando a necessidade de reconhecer e documentar a alteração térmica antropogênica ao estudar e preservar coleções de meteoritos em todo o mundo.

Palavras-chave: Ligas Fe-Ni; Padrão Widmanstätten; Classificação de danos térmicos

1 Introduction

Meteorites are fragments of naturally produced solid material that have survived passage, from interplanetary space, through the Earth's atmosphere and have landed on the surface of the Earth (Hutchison 2004; Norton & Chitwood 2008). Meteoritic material originates predominantly in the belt of asteroids, between Mars and Jupiter, and in many instances the meteorite is obviously a fragment from a large differentiated parent body with an iron-nickel nucleus (Goldstein, Scott & Chabot 2009; Yang, Goldstein & Scott 2010).

As meteorites penetrate the Earth's atmosphere they are decelerated and heated by friction. Most of the frictional or ablational heat is dissipated into the smoke trail that accompanies meteoritic in-fall, and the depth of penetration of ablation heat into the solid meteorite is limited to about one centimeter (Bland & Artemieva 2006).

Metallic meteorites are remnants of planetary cores formed billions of years ago, exhibiting metallographic structures that record extremely slow cooling rates. These natural alloys offer a unique natural context for studying phase transformations and equilibrium behaviors in Fe–Ni alloys undergoing extremely slow cooling idealized in theoretical metallurgy. It is estimated that these meteorites cooled from their molten metallic state at a rate of approximately 1 to 100 °C per million years (Buchwald 1975; Goldstein, Scott & Yang 2009). This natural "heat treatment" leads to the formation of metallic alloys that closely approach the thermodynamic equilibrium predicted by theoretical models. For this reason, metallic meteorites are invaluable specimens for researchers in metallurgy, geosciences, and planetary science, as they exhibit phase transformations that, although extraterrestrial, approximate the ideal behavior foreseen in terrestrial systems.

On September 2, 2018, a tragic fire consumed the National Museum (MN/UFRJ), an event of irreparable loss to science, history, and national memory, several meteorites withstood the flames (Zucolotto et al. 2019). While some specimens were only superficially affected, others displayed significant structural alterations resulting from intense thermal exposure. The heat-imposed transformations are recorded in their internal structures, revealing varying degrees of thermal modification.

Although the scientific literature contains only a limited number of controlled studies on thermal alteration in iron meteorites (Reisener & Goldstein 2003; Goldstein & Short 1967), the available data are sufficient to constrain the temperatures and durations likely experienced by the specimens. Existing experimental and observational work - though scarce – provides a solid framework for interpreting the structural modifications observed in the affected samples. At the same time, it exposes a significant gap in meteoritic metallography and underscores the scientific value of expanding research on heat-induced transformations in Fe–Ni alloys.

The primary objective of this study is to reconstruct, with high microstructural and thermodynamic resolution, the thermal and mechanical overprinting experienced by the metallic meteorites formerly housed in the MN/UFRJ. By integrating classical metallographic principles with contemporary experimental and natural observations, particularly those concerning Widmanstätten growth kinetics, nickel redistribution, accessory-phase stability, and shock-induced deformation (e.g., Wood 1964; Goldstein & Ogilvie 1965; Kase 1925; Vogel 1927, 1932; Perry 1944; Reisener & Goldstein 2003; Yang et al. 2010). The research aims to quantify the extent to which the 2018 fire modified primary asteroidal structures relative to pre-existing cosmic features.

To support this analysis, the study establishes a systematic reference table of temperature-dependent metallographic effects, synthesizing classical experimental data and natural observations. This table serves as a comparative framework for evaluating the thermal implications suffered by individual meteorites within the fire-affected MN/UFRJ collection, enabling consistent assessment of peak temperatures, exposure durations, and thermal gradients. The systematic analysis of diagnostic indicators, including distortion or loss of Widmanstätten lamellae, diffusion-controlled Ni homogenization, phosphide melting and reprecipitation, modification of plessite fields, and temperature-dependent recrystallization, provides a robust basis for the forensic interpretation of iron meteorites subjected to high-temperature terrestrial events and contributes to the development of informed conservation strategies for meteoritic heritage impacted by catastrophic fires.

At the same time, these specimens serve as sensitive recorders of the thermal conditions within the burning structure, offering insights relevant not only to meteoritics but also to the response of associated geological and anthropogenic materials exposed to the same environment. Ultimately, the study advances both the fundamental understanding of Fe–Ni alloy behavior under catastrophic heating, whether of terrestrial or cosmic origin, and the development of conservation and restoration strategies for meteoritic cultural heritage affected by extreme environmental conditions.

2 Meteorite Metallography Review

The mineralogy of iron meteorites reflects a complex sequence of primary crystallization, subsolidus diffusion, shock deformation, and subsequent thermal overprinting. Although the principal phases - kamacite, taenite, graphite, schreibersite, troilite, and various phosphates - were recognized as early as Rose (1864), modern metallographic and microanalytical studies have significantly refined our understanding of their formation and transformation pathways (Buseck 1969; Clarke & Scott 1980). Table 1 summarizes the primary and accessory minerals commonly documented in unweathered iron meteorites.

Iron meteorites are composed predominantly of metallic iron containing approximately 5–20 wt% nickel. Although higher nickel concentrations may occur in some specimens, exceeding 20 wt%, such compositions are relatively uncommon and are exemplified by meteorites such as Santa Catarina (Zucolotto et al. 2013). In addition to the Fe–Ni metallic phases, iron meteorites typically host inclusions of troilite (FeS), schreibersite [$(Fe,Ni)_3P$], and minor chromite, graphite, and carbide minerals such as cohenite [$(Fe,Ni)_3C$]. The metal in iron meteorites typically presents in two phases: kamacite and taenite, occurring in a texture known as the Widmanstätten pattern, which consists of an oriented intergrowth of kamacite and high-Ni taenite regions.

2.1 Fundamental Phase Relations in Fe–Ni Systems

The Widmanstätten pattern is one of the most diagnostically important structural features in iron meteorites. It arises in meteorites that cooled extremely slowly – typically at rates between 1–100 °C per million years – within the cores of differentiated asteroidal bodies (Yang et al. 2010; Goldstein et al. 2009). Its presence reflects not only chemical composition but also the thermal and mechanical history recorded in the Fe–Ni alloy system.

In iron meteorites, the Widmanstätten pattern is expressed through the intergrowth of two major Fe–Ni phases: ferrite (kamacite, α-FeNi) and austenite (taenite, γ-FeNi). Kamacite lamellae nucleate and grow within a taenite host, producing the characteristic geometric pattern. The Fe–Ni phase diagram governs the phase transformation pathways (Massalski et al. 1990), solvus limits, and diffusion-controlled formation of taenite rim zoning, as well as the development of plessite – a fine intergrowth of α+γ phases that forms during the decomposition of residual taenite (Goldstein & Michael 2006). Together, these features provide key constraints on cooling rates, parent-body structure, and the physicochemical conditions prevailing during metallographic evolution.

2.1.1. Formation of the Widmanstätten Pattern

The Widmanstätten pattern results from the exsolution of kamacite (α-Fe[Ni], body-centered cubic -bcc- ferrite) from an originally homogeneous taenite (γ-Fe[Ni], face-centered cubic -fcc- austenite) matrix as the alloy cools

Table 1 Primary and Accessory Minerals in Iron Meteorites. Adapted from Buchwald (1975).

Mineral	Formula	Structural System	Notes
Kamacite	α-Fe(Ni)	BCC	Ni < 7.5 wt%; main cooling phase
Taenite	γ-Fe(Ni)	FCC	Ni > 25 wt%; decomposes into plessite
Schreibersite/Rhabdite	$(Fe,Ni)_3P$	Tetragonal	Forms thorns, spherules, eutectics
Troilite	FeS	Hexagonal	Shock-melt sensitive; eutectics
Cohenite	$(Fe,Ni)_3C$	Orthorhombic	Decomposes to kamacite + graphite
Haxonite	$(Fe,Ni)_{23}C_6$	Cubic	Same alterations as cohenite
Graphite	C	Hexagonal	Derived from carbide decomposition
Daubreelite	$FeCr_2S_4$	Cubic	Present in troilite inclusions
Chromite	$FeCr_2O_4$	Cubic	Accessory in many irons
Silicates	Various	—	Common in silicate-bearing Irons

under astronomically slow cooling rates through the α + γ two-phase field of the Fe–Ni phase diagram (Goldstein, Scott & Yang 2009) (Figure 1). During the extremely slow cooling of iron meteorite parent bodies at temperatures between approximately 450 and 700 °C, the formation of the Widmanstätten pattern is controlled by the diffusion of nickel in the taenite phase.

The precipitation of kamacite occurs through the exsolution of Ni-poor bcc iron from the Ni-rich fcc taenite, with kamacite plates growing along specific crystallographic planes determined by the lattice orientation. Kamacite nucleates from homogeneous taenite after undercooling, and its plate-like growth proceeds with broad habit planes parallel to the {111} octahedral planes of the parent taenite. Because each meteorite crystal contains multiple crystallographic orientations, the kamacite grows in an octahedral framework, producing the familiar interpenetrating set of plates seen in two dimensions as lamellae (Buchwald 1975).

2.1.2. Microscopic Components of the Widmanstätten Structure

The microscopic components of the Widmanstätten structure include:

Kamacite bands: broad, low-Ni α-phase lamellae with typical concentrations of 5.0–7.5 wt% Ni. Kamacite commonly exhibits compositional zoning with a narrow Ni depletion at the kamacite–taenite interface (the "Agrell effect" – Figure 2), reflecting diffusional equilibration during slow cooling (Goldstein et al. 2009). Kamacite commonly contains inclusions of phosphides (schreibersite, rhabdite), graphite, and troilite, with grain boundaries and deformation substructures decorated by phosphide precipitates formed during cooling or subsequent annealing (Buchwald 1975).

Taenite ribbons: high-Ni γ-phase layers, typically containing 20–40 wt% Ni. Taenite lamellae bordering kamacite define the Widmanstätten pattern in octahedrites; their morphology, width, and Ni gradients remain among the most important indicators of the cooling history of iron meteorites (Yang et al. 2007). The growth of the Widmanstätten pattern is controlled by the diffusion of Ni in the taenite.

Plessite fields: fine-scale mixtures formed from the decomposition of residual taenite, ranging from martensitic structures to micro-Widmanstätten

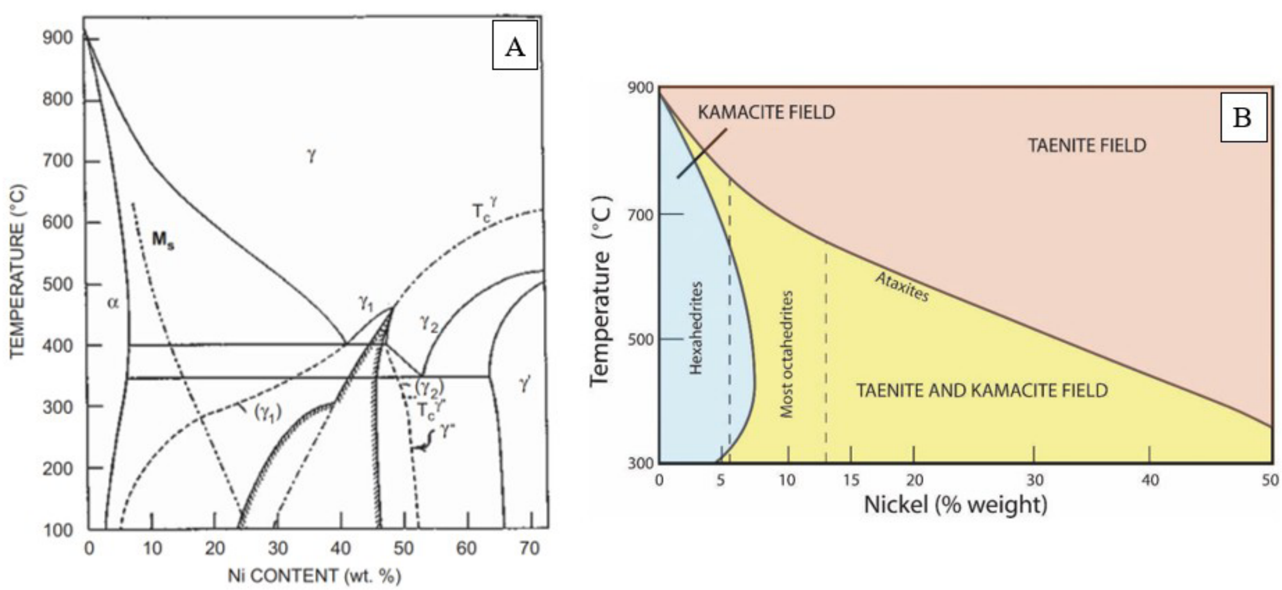

Figure 1 A. Fe-Ni binary phase diagram (from Yang et al. 1996). α is low-Ni bcc phase, γ a high-Ni fcc phase, $γ_1$ a low-Ni paramagnetic fcc phase, $γ_2$ a high-Ni ferromagnetic fcc phase, γ' is ordered Ni_3Fe, γ" is ordered FeNi-tetrataenite, and M_s is the martensite starting temperature. $T_c^γ$ is the Curie temperature of the γ phase; B. Simplified schematic Fe–Ni phase stability diagram (from Norton & Chitwood 2008) illustrating the stability fields of kamacite, taenite, and the two-phase kamacite + taenite region as a function of temperature and bulk nickel content. The diagram highlights the compositional ranges typical of major structural classes of iron meteorites, including hexahedrites (low-Ni), octahedrites (~6.5–10.5 wt% Ni), and ataxites (high-Ni), and provides a metallographic framework for interpreting Widmanstätten pattern development and thermal overprinting.

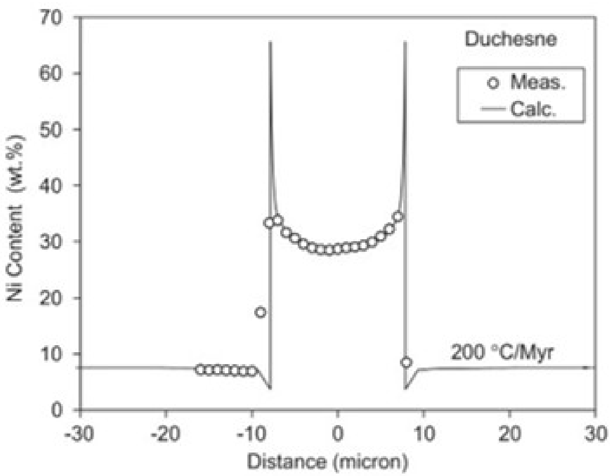

Figure 2 Comparison between measured and calculated Ni profiles across the kamacite – taenite phases (from Goldstein et al. 2009). Showing the “Agrell effect” in kamacite and M-curve profile in taenite.

intergrowths. Plessite represents an intergrowth of kamacite and taenite phases formed from the diffusionless transformation (martensite reaction) of taenite during cooling, or from reheating and subsequent reequilibration. Plessite textures are classified into multiple types based on their morphologies and nickel contents, ranging from cellular to duplex structures, and their presence and characteristics provide additional constraints on the cooling and impact histories of iron meteorites (Reisener & Goldstein 2003).

Cloudy taenite: corresponds to a nanometer-scale intergrowth produced by spinodal decomposition of taenite during the final stages of cooling below ~400-450 °C. This process generates a heterogeneous mixture of ordered tetrataenite ($L1_0$-FeNi) and Ni-poor precipitates, forming the characteristic “cloudy zone” along taenite rims (Buchwald 1975; Goldstein & Michael 2006). The width and microstructural complexity of this zone vary inversely with cooling rate, making it one of the most reliable indicators of subsolidus thermal histories in iron meteorites (Goldstein et al. 2009; Yang et al. 1996). Tetrataenite domains range from >500 nm to <10 nm depending on Ni content and diffusional pathways, and their high coercivity allows preservation of stable remanent magnetization, providing direct constraints on the paleomagnetic field of the parent body (Bryson et al. 2015).

These components arise in a temperature-dependent sequence and provide direct information on the cooling rate and thermal stability of the host meteorite.

2.1.3. Growth Mechanisms and Nickel Redistribution

Metallographic and diffusion studies, beginning with the pioneering models of Wood (1964) and later refined by Goldstein & Ogilvie (1965), Willis & Goldstein (1981), and more recently by Yang & Goldstein (2005), demonstrate that the Widmanstätten structure develops by diffusion-controlled growth. As kamacite nucleates, it rejects nickel, which diffuses into the surrounding taenite. Because Ni diffuses much more slowly in the γ phase than in the α phase, the rate-limiting step is Ni migration within taenite (Goldstein et al. 2009).

As cooling continues, diffusion profiles evolve through distinct stages:

1. Initial nucleation at a temperature slightly below the equilibrium ($\gamma \rightarrow \alpha + \gamma$) boundary (Wood 1964);
2. One-dimensional growth of kamacite plates with nearly uniform composition (Goldstein & Ogilvie 1965);
3. Development of M-shaped Ni profiles in adjacent taenite due to overlapping diffusion fields (Yang et al. 2010) (Figure 3);
4. Late-stage interface equilibration, producing Ni-depleted rims in kamacite (the “Agrell effect”) (Buchwald 1975).

The thickness of kamacite lamellae (band width) depends on the balance between cooling rate, initial Ni content, and diffusion kinetics (Goldstein et al. 2009; Yang & Goldstein 2005). This relationship provides a powerful tool for constraining thermal histories independently from radiometric ages. Cooling rate data can be obtained through diffusion-controlled Ni concentration profiles in both kamacite and taenite, with cooling rates generally lying in the range of 1–100 °C per million years for cooling through the temperature range of approximately 500 °C.

2.2 Accessory Minerals and Phases

Accessory minerals in iron meteorites record both primary crystallization and post-formation modification. Their behavior during thermal overprinting provides

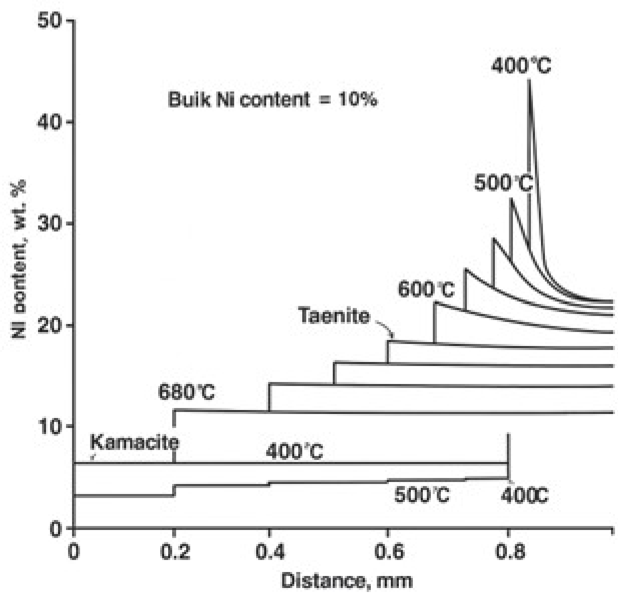

Figure 3 The computed development of Ni profiles in a cooling octahedrite (from Wood 1968). Left edge of figure represents midpoint of a kamacite lamella; kamacite expands and increases in Ni content as temperature falls. Right edge of figure is center of a residual taenite area. Here, the Ni content also increases, at first throughout the taenite, later along edges only. Final result is an M-shaped profile.

key constraints on heating events, including cosmic reheating, impact-generated shock, and anthropogenic high-temperature disturbances (Buchwald 1975; Goldstein et al. 2009).

Schreibersite and Rhabdite [$(Fe,Ni)_3P$]: Phosphide minerals occur as both large skeletal crystals and tiny rhabdite needles. Their morphology and interfaces with kamacite provide sensitive indicators of thermal history and reheating conditions. Slow reheating produces partial spheroidization and taenite segregation along interfaces (Ruzicka & Hutson 2010). Short, intense reheating generates "thorny" boundaries - unequilibrated phosphorus-rich subboundaries projecting into kamacite. Selective melting at temperatures >1000 °C produces rounded voids, phosphorus-rich eutectics, and steadite textures (Buchwald 1975).

Troilite (FeS) and Sulfide Assemblages: Troilite is the dominant sulfide in iron meteorites, commonly occurring as massive nodules or thin lamellae aligned with kamacite–taenite boundaries. Under localized shock heating, troilite may melt selectively, producing Fe–S eutectic structures whose coarseness reflects the degree of contamination by adjacent metal (Ramdohr 1967). If melting is minimal and compositionally pure, troilite recrystallizes into equiaxed, randomly oriented grains. Increasing incorporation of metal yields finer-grained eutectic textures. More intense heating leads to partial or complete destruction of troilite–daubreelite intergrowths, dispersing daubreelite grains into sulfide melt (Ruzicka et al. 2014).

Carbides – Cohenite [$(Fe,Ni)_3C$] and Haxonite [$(Fe,Ni)_{23}C_6$]: Carbides form late in the primary cooling sequence but are metastable over geologic time and are particularly sensitive to thermal overprinting. Slow annealing (<500 °C) produces decomposition to kamacite + graphite, yielding columnar ferrite and lamellar graphite (Reed 1965). Short reheating in atmospheric or shock zones (700–900 °C) produces carbon diffusion into austenite, yielding bainitic or martensitic halos after cooling (Yang et al. 2010). Intense brief reheating (>1100 °C) produces selective melting of carbides and formation of ledeburitic textures upon rapid cooling. These transformations are best preserved in Canyon Diablo and several group I and IIIA meteorites where multiple reheating episodes have occurred (Buchwald 1975).

2.3 Iron Meteorite Classification

Structural Classification: Meteorites that contain approximately 7–11 wt% Ni are most likely to develop well-defined Widmanstätten structures and are correspondingly classified as octahedrites, whose characteristic intergrowths of kamacite and taenite define their subtypes based on kamacite bandwidth (Table 2). Low-Ni irons (~5.5 wt% Ni) may consist almost entirely of single-phase α-Fe and are classified as hexahedrites. High-Ni irons (>14 wt% Ni) often lack macroscopic structural features and are designated ataxites, despite commonly preserving fine-scale plessitic textures. Octahedrites are the most common iron meteorites recovered on Earth, accounting for the vast majority of meteorite falls (Buchwald 1975; Scott & Wasson 1976).

Chemical Classification: Modern classification of iron meteorites is founded primarily on chemical composition, reflecting the need to understand the conditions under which these objects formed and differentiated. Iron meteorites are currently divided into thirteen chemical groups, based mainly on variations in nickel (Ni), phosphorus (P), and a suite of trace elements, particularly gallium (Ga), germanium (Ge), and iridium (Ir). These elements were first identified as key discriminators by Goldberg et al. (1951), Lovering et al. (1957), Wasson (1967; 1974), and Wasson & Kimbeblin (1967). The chemical groups are distinguished largely by decreasing Ga and Ge abundances

Table 2 Iron meteorite structural classes (after Buchwald 1975). Structural classification based on kamacite bandwidth, approximate nickel content, and representative meteorites.

Structural class	Symbol	Ni (wt%) approx.	Bandwidth (mm)	Meteorite example
Hexahedrite	H	5.5	–	Coahuila
Coarsest octahedrite	Ogg	6	> 3.3	Sikhote Alin
Coarse octahedrite	Og	7	1.3–3.3	Canyon Diablo
Medium octahedrite	Om	8	0.5–1.3	Cape York
Fine octahedrite	Of	9	0.2–0.5	Gibeon
Finest octahedrite	Off	9–18	< 0.2, continuous	Tazewell
Plessitic octahedrite	Opl	10	< 0.2, sparks	Ballinoo
Ataxite	A	16	–	Hoba
Anomalous	Anom	5–40	diverse	Morradal

– from roughly 100 ppm Ga (Group I) down to <1 ppm Ga (Group IV), with numerous trace elements showing systematic positive or negative correlations with Ni and Ga.

Both structural and chemical classifications show strong correspondence, particularly when both macrostructure and microstructure are considered. Importantly, the adoption of chemical classification does not replace earlier structural schemes; rather, they complement one another to provide comprehensive characterization of each iron meteorite specimen.

For this reason, Buchwald (1975) proposed that each iron meteorite should be defined by a combined “fingerprint”, consisting of:

- **Structural class**, e.g., “medium octahedrite, kamacite bandwidth of 0.9 ± 0.1 mm”;
- **Bulk composition**, including at minimum Ni and P, and ideally the trace elements Ga, Ge, and Ir.

Finally, although nickel distribution in iron meteorites spans roughly 5–20 wt%, its frequency is highly irregular as the global Ni distribution is not a single continuous population, but instead the superposition of several distinct geochemical groups, each with its own internal coherence (Table 3).

2.4 Shock Effects and Mechanical Deformation

Shock deformation significantly modifies the crystalline structure of iron meteorites and is most visibly expressed through Neumann bands and high-pressure polymorphic transformations (Yang et al. 2010).

Neumann Bands and Mechanical Twins: Neumann bands (Neumann lines) are mechanical twins in kamacite formed under shock pressures below ~130 kbar (Cohen 1905; Buchwald 1975). They occur in hexahedrites, octahedrites, and even ataxites where the kamacite exceeds 20–50 µm in thickness. Their density, geometry, and distribution provide diagnostics of past shock deformation. Neumann bands are indicative of a shock-induced deformation of the kamacite crystal, and are generally attributed to impact events on the parent body of the meteorite.

High-Pressure Shock Transformations: Under higher shock pressures (>130 kbar), kamacite partially transforms to hexagonal ε-Fe. Rapid back-transformation to α-Fe produces a distinctive densely cross-hatched structure resembling martensite, typically accompanied by elevated microhardness (up to ~320 VHN) (Buchwald 1975; Scott & Wasson 1975). These shock-generated $\alpha \rightarrow \varepsilon$ structures have been synthesized experimentally and serve as reliable indicators of extreme shock metamorphism (Langenhorst 2002).

2.5 Thermal Modification of Iron Meteorites

Secondary thermal histories in iron meteorites produce diagnostic microstructural changes that can be used to reconstruct reheating paths and cooling conditions (Langenhorst 2002). Secondary metallographic features have been recognized since the classical work of Sorby (1887) and were subsequently refined by Cohen (1905), Berwerth (1914) and Perry (1944), and later by Axon (1963), Goldstein & Ogilvie (1965), Buchwald (1975) and Yang & Goldstein (2005), who demonstrated that specific microstructural responses are tightly linked to both the peak temperature and the duration of heating.

Perry’s (1944) experimental and observational work established that the earliest indicators of thermal modification occur in the α-phase (kamacite). Neumann lines begin to blur, widen and ultimately disappear under

Table 3 Properties of 13 groups of iron meteorites and the ungrouped irons.

Group	Number	Ni (wt%)	Structure[a]	Example	Reference
IAB[b]	387	6–60	Og-D	Canyon Diablo	Choi et al. (1995)
IC	14	6–7	Ogg, Og	Bendegó	Scott & Wasson (1976)
IIAB	154	5.3–6.8	H, Ogg	Coahuila	Wasson et al. (2007)
IIC	8	9.3–11.5	Opl	Baliñoo	Wasson (1969)
IID	31	9.6–11.1	Om, Of	Carbo	Wasson & Huber (2006)
IIE	26	7.2–9.5	Og-Off	Weekeroo	Wasson & Wang (1986)
IIF	8	9.1–11.4	Opl, D	Corowa	Kracher et al. (1980)
IIG	6	4.1–4.9	H	Bellsbank	Malvin et al. (1984)
IIIAB	366	7.1–10.6	Om	Cape York	Wasson (1999)
IIIE	22	8.1–9.6	Og	Kokstad	Malvin et al. (1984)
IIIF	9	6.8–8.5	Og, Om	Clark Co.	Kracher et al. (1980)
IVA	94	7.5–12	D	Gibeon	Wasson & Richardson (2001)
IVB	18	16–18	D	Hoba	Walker et al. (2008)
Ungrouped[b]	160	6–35	Og-D	Butler	Wasson (1990)

Obs.: Based largely on the listed references and the Meteoritical Bulletin Database: http://tin.er.usgs.gov/meteor/metbull.php. Numbers exclude paired specimens and irons with tentative classifications.

[a] **Structure:** H, hexahedrite; Ogg, Og, Om, Of, Off - coarsest, coarse, medium, fine, and finest octahedrites; Opl, plessitic octahedrite, D, ataxite. See Buchwald (1975, Table 26a) for definitions.

[b] **Wasson** and Kallemeyn (2002) define 120 irons from groups IAB and IIICD and ~35 ungrouped irons as a "group IAB complex". IIIC and IIID irons are included in their scheme as sLM and sLH subgroups, respectively. The silicate-bearing groups IAB and previous IIICD (now IAB) did not form by fractional crystallization.

prolonged exposure in the range of ~550–600 °C, and may even degrade slowly at temperatures as low as ~400 °C. More intense or sustained heating produces secondary granulation of kamacite, partial to advanced diffusion of schreibersite and progressive alteration of dense plessite fields. At still higher temperatures, approaching or exceeding ~1000 °C, schreibersite begins to melt and Widmanstätten lamellae undergo severe distortion or complete obliteration, effects well documented in both natural reheating and laboratory treatments described by Kase (1925) and Vogel (1927, 1932).

Perry (1944) emphasized a fundamental distinction between terrestrial reheating, brief and superficial, occurring during atmospheric passage, and cosmic reheating, which can act on the entire volume of the meteorite. Terrestrial heating at atmospheric entry produces only a shallow "zone of alteration" a few millimeters to about one centimeter thick, characterized by dull granular etching, loss of Neumann lines and minimal diffusion of taenite and phosphides, while the interior remains essentially unaffected. In contrast, cosmic reheating can extensively modify the bulk structure, transforming hexahedrites into nickel-poor ataxites through whole-mass granulation and diffusion of taenite and phosphides.

Historical observations show that incidental heating of iron meteorites rarely produces measurable microstructural alteration. Specimens such as Hammond and the Troost iron were intentionally heated in forges for analytical purposes, yet no convincing structural modifications were documented, and the Rafriiti meteorite, reportedly heated for years near a domestic stove, likewise exhibited no detectable changes. Laboratory experiments indicate that prolonged heating near 400 °C may initiate very early granulation (Tammann temperature), but practical conditions capable of producing even incipient granulation in kamacite require temperatures of at least ~550 °C sustained for many hours (Kase 1925). Significant transformations, such as melting of schreibersite, would only occur close to 1000 °C, corresponding to bright red to orange heat. The Cedartown hexahedrite provides a striking example: although recovered from the ashes of a house fire and presumably exposed to dull-red heat, it showed no microstructural alteration, with no granulation, no schreibersite diffusion and perfectly preserved Neumann lines (Perry 1944).

Terrestrial reheating during atmospheric passage, therefore, is brief and produces only superficial changes, forming the well-known alteration zone. This peripheral band, typically up to about one centimeter thick, shows dull granular etching, loss of Neumann lines, granulation of kamacite and partial diffusion in plessite and schreibersite. The depth of modification is small because heating is short-lived and the interior remains cold; even thin taenite lamellae are usually unaffected. Experimental data indicate that only a few seconds near ~1000 °C are required to produce such incipient changes. Atmospheric heating also generates a thin magnetic-oxide fusion crust that may penetrate surface cracks, whereas cosmic reheating affects the entire mass and results in widespread structural modification.

Neumann lines are highly sensitive to heat and represent one of the earliest visible indicators of thermal alteration in iron meteorites. Upon heating within the upper α-phase field, the lines widen, distort and gradually merge with developing grain boundaries until they disappear during secondary granulation. Experimental studies show that prolonged annealing at ~550–560 °C is sufficient to obliterate Neumann lines, and even slower degradation may occur at temperatures as low as ~400 °C. Their preservation therefore indicates an absence of significant terrestrial reheating, whereas their destruction marks exposure to elevated temperatures. Because schreibersite begins to diffuse near ~700 °C and melts around ~970 °C, any heating capable of altering phosphide inclusions would necessarily erase pre-existing Neumann lines.

Because thermal alteration is strongly dependent on time and temperature, brief reheating episodes can nevertheless profoundly affect taenite. Exposure of taenite to temperatures above ~700–800 °C softens the phase and modifies its optical appearance. Carbon, formerly in solid solution, redistributes during heating, and subsequent rapid cooling produces bainitic–martensitic structures in adjacent metal. This behavior, documented in several irons such as Kayakent and Cape York, is also characteristic of heat-affected rim zones and can even appear in shock-reheated samples of Canyon Diablo.

The cloudy or stained taenite typical of submicroscopic α+γ mixtures becomes optically clear and yellow, often passing through an intermediate mosaic texture. This transition reflects the transformation of the original nanometric α+γ intergrowths into homogeneous γ that remains metastable upon rapid cooling. Such textures are ubiquitous in meteorites subjected to significant thermal overprinting.

Experimental annealing confirms the extreme sensitivity of taenite to heating: 15 days at 500 °C, 10 minutes at 800 °C, or even 10 seconds at 900 °C produce comparable softening and microstructural modification. These results highlight the rapid rate at which taenite records thermal excursions and reinforce its diagnostic value for reconstructing high-temperature events, whether atmospheric, cosmic, or anthropogenic, as in the case of the 2018 MN/UFRJ fire.

The thermal response of iron meteorites to heating has been systematically documented through controlled experiments and natural reheating events, as summarized in Table 4. This compilation provides a quantitative framework for distinguishing superficial atmospheric alteration from pervasive cosmic or anthropogenic overprinting, enabling precise reconstruction of secondary thermal histories in meteoritic Fe-Ni alloys.

3 Materials and Methods

The methodology adopted for the recognition, stabilization, and assessment of recovered metallic meteorites combined classical metallographic approaches with modern analytical techniques, supported by expertise in mineralogy and petrology, following established procedures in the literature (Perry 1944; Buchwald 1975; Scott & Wasson 1975; Zucolotto et al. 2013; Monteiro 2018). Initial recognition involved macroscopic evaluation of physical attributes such as mass, size, morphology and surface texture, combined with comparison to pre-fire photographic databases and catalogue records. Recovered items were preliminarily grouped as identified, suspected or unidentified specimens (Monteiro et al. 2020).

All samples underwent metallographic preparation, including cutting, grinding, polishing and chemical etching to reveal diagnostic features such as Widmanstätten patterns and Neumann bands. Optical and metallographic observations were performed using binocular lenses and petrographic and metallographic microscopes. When visual and metallographic criteria were insufficient for definitive identification, quantitative chemical analyses were conducted using a Bruker Tracer 5i Handheld X-ray Fluorescence (HHXRF) (Zucolotto et al. 2022).

Optical imaging was carried out under reflected light using a ZEISS Axioplan microscope equipped with an AxioCam ICc 3 digital camera at the LABSONDA facility (IGEO/CCMN/UFRJ). Quantitative EPMA analyses were performed using a JEOL JXA-8230 microprobe (20 kV, 20 nA, 1 µm beam diameter), generating backscattered electron (BSE) images and complemented by EDS analyses.

Approximately 400 specimens were recovered, of which about 150 could be identified based on mass, type and comparison with the pre-fire database, despite limitations imposed by outdated catalogue records and extensive fragmentation. Samples were cleaned, stabilized and stored according to catalogue numbering, with silica

Table 4 Temperature–dependent microstructural changes in iron meteorites (after Perry 1944, Buchwald 1975 and Yang et al. 2011).

Temperature Range	Expected Microstructural Changes	Diagnostic Indicators
~300–550 °C (prolonged exposure)	● Very early diffusion processes; ● Slight degradation of plessite.	● Neumann lines begin to weaken; ● Recovery of kamacite; ● Subgrain formation in kamacite.
~550–600 °C (hours to days)	● Secondary granulation in kamacite; ● Progressive disappearance of Neumann lines.	● Neumann lines widen, distort and eventually disappear; ● Kamacite grains begin to subdivide; ● Early diffusion of schreibersite begins.
600-700 °C	● Clear secondary granulation; ● Disruption of taenite lamellae.	● Transformation of plessite to decomposed martensitic textures.
~700–800 °C	● Clear diffusion of phosphides and taenite; ● Alteration of plessite fields; ● Dense plessite becomes coarser and loses definition.	● Schreibersite develops thorny outlines and partial melting begins; ● The cloudy or stained taenite simultaneously becomes clear and yellow.
800-900 °C	● Kamacite will transform in α_2	● Beginning loss of Widmanstätten clarity in coarse octahedrites
~900–970 °C	● Strong diffusion regime; ● Destabilization of taenite lamellae; ● Sulphide will form eutectics.	● Taenite begins to lose sharp boundaries; ● Kamacite grains granulate extensively; ● Octahedral structure becomes discontinuous.
~970–1100 °C	● Melting of schreibersite; ● Metal becomes nearly homogeneous.	● Phosphide inclusions melt and produce rounded cavities; ● Kamacite loses structural integrity; ● Recrystallization dominates.
1100-1300 °C	● Severe whole-mass modification; ● High diffusion of Ni; ● Phosphides and taenite Widmanstätten pattern seriously degraded or obliterated.	● Total loss of the original octahedral texture; ● Widmanstätten pattern destroyed.
>1300 °C	● Formation of fusion crust–like features and dendritic recrystallization; ● Melting of natural magnetite–iron oxide mixtures).	● Dendritic iron droplets enclosed by magnetic oxide (“intrusive oxide”); ● Evidence of high thermal gradients with rapid cooling; ● Structures similar to fusion crusts or oxide-filled bays.
Terrestrial atmospheric reheating (seconds)	● Fusion crust and intrusive oxide in cracks; ● Shallow “zone of alteration” (mm to 1 cm).	● Surface dull, granular etching; ● Loss of Neumann lines near edge; ● Minimal diffusion.

gel used to mitigate ongoing oxidation. Specimens were preliminarily organized by mass and type (metallic, stony or mixed), while thin sections were prepared for samples exceeding 10 g to allow definitive identification and reclassification through EPMA. Recovery efficiency was strongly mass-dependent, with nearly complete recovery for specimens >1 kg and progressively lower recovery rates for smaller fragments.

4 Fire Impact Assessment, Thermal Damage Classification, and Post-Fire Recovery of the Meteorite Collection of the MN/UFRJ

The fire that destroyed the main building of the National Museum of Rio de Janeiro (MN/UFRJ) on September 2nd, 2018 caused different degrees of damage to the meteorites, depending on where they were located at the time of the incident. The specimens were distributed across three distinct areas with increasing fire intensity: (1) the main entrance hall; (2) the exhibition space adjacent to the entrance; and (3) the collection area along the back aisle of the building.

At the main entrance (1), where the Bendegó main mass meteorite was displayed, there was no direct impact from the fire; consequently, neither the meteorite nor any other element in that room sustained thermal damage. The specimen was only covered by soot and debris from the ceiling.

The exhibition hall (2) experienced only mild effects, as the few wooden and acrylic display structures were the only combustible materials present. As the meteorites were recovered the following day by the curator (the second author), lying only among ashes and debris from the ceiling.

The back aisle (3) was the most severely affected sector of the building. There was no water supply in that area, and no firefighting efforts could be carried out. As a result, the wooden upper floors, furniture, shelves, and the roof collapsed onto the shelving units where the collection was stored, and the wooden structures continued burning throughout the night.

The meteorites were housed in four different shelving types: one composed of fire-resistant iron drawers, two made of thick glass shelves, and another consisting of wooden drawers covered by thin glass. All units were positioned along the walls. This environment exposed the meteorites to elevated, but highly variable, temperature gradients. Consequently, the specimens were heterogeneously affected.

The access to the collection area had to wait seven-weeks to be liberated by the federal police. The absence of a protective structure allowed repeated direct exposure to rainfall. This uncontrolled hydration–dehydration cycling, combined with the presence of soluble salts and corrosion-promoting residues from burned materials, accelerated oxidation and secondary mineral formation in meteorites.

The intention is to use the iron meteorites as a reference framework to evaluate the extent of thermal damage sustained by the collection, since the Fe–Ni metallurgical system in meteorites exhibits well-characterized microstructural behavior. Because the thermal evolution of kamacite, taenite, plessite, and phosphides occurs in predictable and temperature-dependent stages, the iron meteorites provide a reliable comparative standard. This metallurgical knowledge allows us to correlate specific microstructural modifications, such as diffusion features, granulation, phase destabilization, and the degradation of the Widmanstätten pattern, with the range of temperatures experienced during the fire.

In addition to the thermal overprint, rapid development of corrosion products was observed. Several specimens display advanced oxidation fronts progressing along microfractures and pre-existing structural weaknesses created by the collapse, significantly intensifying the post-fire alteration and complicating the reconstruction of their original microstructural characteristics.

4.1 Recovery, Identification, and Reassembly Protocols

Recovery operations extended over approximately three months after that proceed systematic identification, stabilization, and cataloging of each specimen based on pre-fire documentation, macroscopic characteristics, and diagnostic metallographic criteria. This process has been essential for restoring the scientific integrity of the collection and for enabling post-fire analytical studies.

5 Results and Discussions

5.1 Microstructural Framework for Interpreting Reheating in the MN/UFRJ Iron Meteorites

To constrain the thermal overprint imposed by the 2018 fire on the MN/UFRJ meteorite collection, it is necessary to distinguish between the primary meteoritic microstructures and the secondary features produced by fire reheating and subsequent alteration. Following the approach developed for reheated iron meteorites we interpret the present microstructures as a combination of: (i) the original Widmanstätten pattern formed during slow cooling on the parent body, and (ii) modifications induced by the building fire and its aftermath.

In our case, reheating is clearly terrestrial, short-lived (on the order of hours), and accompanied by oxidizing and chloride-rich conditions, rather than impact-related and long-lasting over 10^2–10^4 years.

A range of diagnostic features was observed in fire-affected MN/UFRJ meteorites (Figures 4-10), consistent with experimental and natural studies of reheated Fe–Ni systems: Terrestrial heating produces the familiar ‘zone of alteration’, a feature that has been recognized and interpreted since early metallographic studies, prior to the development of modern analytical methods.

5.2 Spatial Distribution of Thermal Effects

The degree of alteration observed within the MN/UFRJ meteorite collection correlates directly with the spatial distribution of specimens within the building at the time of the fire, as well as with the structural behavior of each sector during combustion and collapse. Three distinct levels of thermal impact were recognized.

The Bendegó iron meteorite, prominently displayed at the museum’s main entrance, in a sector that did not experience direct fire exposure, is classified as Level 0. It remained completely unaltered and now serves as a critical reference for pristine meteoritic metal (Figure 4A,C).

Level 1 corresponds to the exhibition area adjacent to the Bendegó meteorite, where metallic meteorites experienced minimal thermal exposure. The exhibition context prior to the fire, the condition of the area on the morning following the event, and the field recovery of specimens at ambient temperature are documented in Figure 11A-C. A total of thirty (30) out of thirty-nine (39) displayed

Figure 4 A. The Bendegó meteorite on the day following the fire, demonstrating the absence of thermal damage. The poster behind the specimen and the wooden elements in front of it remained intact, with no visible signs of burning; ceiling debris is observed on the floor; B. A Bendegó fragment stored in the collection area, partially covered by molten glass; C. Polished and etched (2 % nital) section of Bendegó meteorite prior to the fire, showing abundant prismatic rhabdites; D. Polished and etched (2 % nital) section of Bendegó meteorite after thermal exposure, in which phosphides develop thorny morphologies and partial melting is observed, while kamacite shows transformation toward the α_2 phase under reflected-light microscopy.

meteorites were recovered on the morning after the fire by the Meteorite Curator (second author of this article), significantly limiting the progression of post-fire secondary weathering (Figure 11D). Metallographic examination of the Carlton iron meteorite recovered from this sector reveals a well-preserved Widmanstätten pattern with no detectable microstructural modification attributable to heating (Figure 11E-F). The inferred thermal profile for this area indicates moderate peak temperatures (≤ 400 °C), followed by rapid air cooling (Figure 11G).

In contrast, Level 2 comprises meteorites stored in the rear collection laboratory, which were subjected to intense and spatially heterogeneous thermal conditions following structural collapse (Figure 12). Progressive metallographic modification is clearly documented in the Pará de Minas and Itutinga iron meteorites, which exhibit blurring and loss of Neumann lines, recrystallization of kamacite, and destabilization of taenite after the fire (Figures 5B-E and 6B, respectively).

Additional evidence for increasing thermal overprint is provided by the Cratheus iron meteorite. Pre-fire reference microstructures display sharp phosphide boundaries and well-defined Widmanstätten features (Figure 7A-F), whereas post-fire samples show diffuse schreibersite boundaries, redistribution of Ni and P, and partial disappearance of phosphide phases due to annealing (Figure 8A-F).

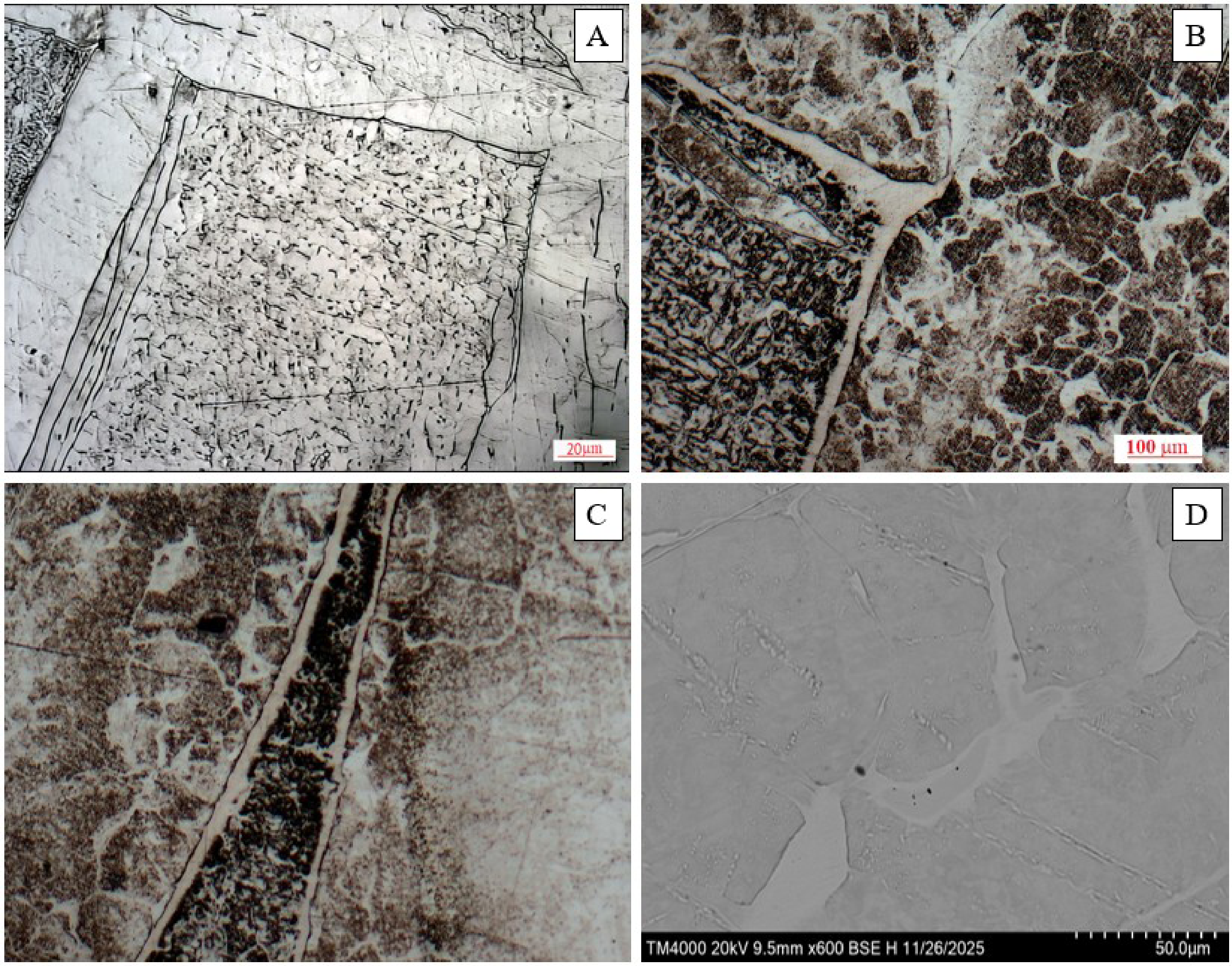

Figure 5 Pará de Minas iron meteorite, polished and etched with 2% nital, showing a fine Widmanstätten structure: A. Pre-fire microstructure, with kamacite bands displaying well-defined Neumann lines, plessite fields and taenite in multiple morphologies; B. Post-fire microstructure; C. Spotted and diffuse appearance produced by artificial reheating. Buchwald interpreted similar structures in the Troost iron as an original α+γ intergrowth partially transformed into a polygonal network of austenite grains by heat treatment at approximately 900–1000 °C. Under limited time–temperature conditions, complete homogenization is prevented, and blurred, undissolved γ particles remain visible; D. SEM image showing progressive blurring and loss of definition in taenite.

Similarly, the São João Nepomuceno meteorite preserves distinct pre- and post-fire states: prior to the fire, asymmetric M-shaped Ni profiles across taenite and martensitic plessite fields are evident (Figure 9A-C), whereas post-fire samples reveal recrystallized kamacite lamellae, darkened grain boundaries, and evidence for carbon redistribution adjacent to taenite (Figure 9D,F).

Although active combustion within the museum structure persisted for only minutes to several hours and did not exceed approximately six hours, as no flames were observed on the following morning, the meteorites were exposed to elevated temperatures for a much longer period beneath collapsed debris. Thermal insulation likely resulted in slow post-fire cooling lasting up to 48–72 hours, a regime incompatible with rapid quenching and instead favoring diffusion-controlled re-equilibration.

Based on these observations, three principal levels of thermal damage were defined and systematically organized in Table 5, correlating fire exposure conditions with their corresponding metallographic responses. Within this framework, a thermal gradient classification expressed through fire-damage stages F0–F7 is proposed, spanning from unmodified material (F0) to complete melting and resolidification of the metallic mass (F7). The progressive

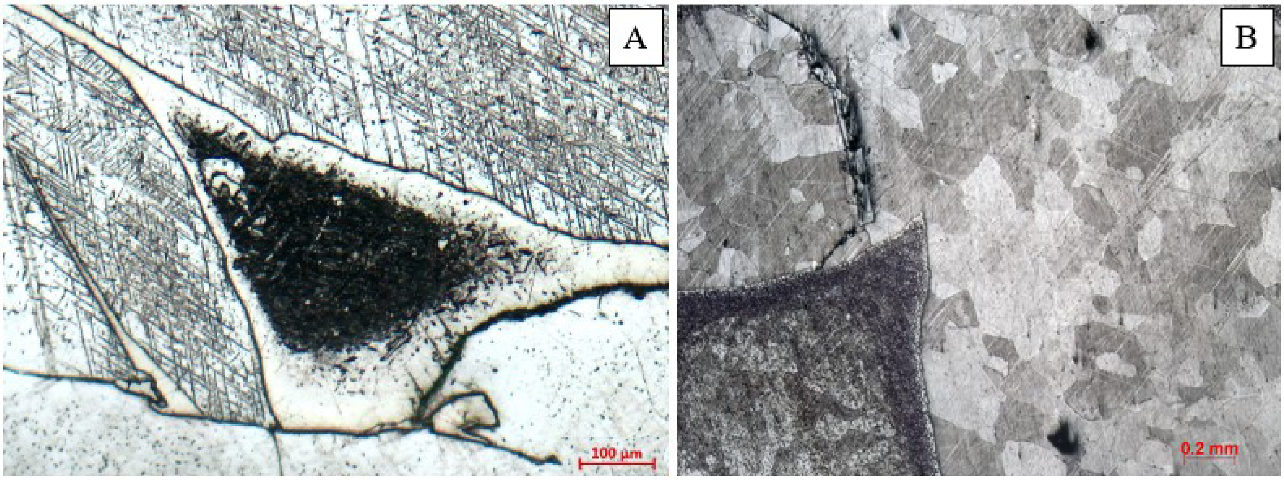

Figure 6 Itutinga iron meteorite, reflected light micrographs of polished and etched with 2% nital, showing a fine Widmanstätten structure: A. Pre-fire microstructure displaying a cross-hatched pattern in kamacite - typical of heavily shocked material - with plessite fields exhibiting taenite rims and dark interiors; B. Post-fire microstructure showing complete recrystallization of kamacite into equiaxed grains.

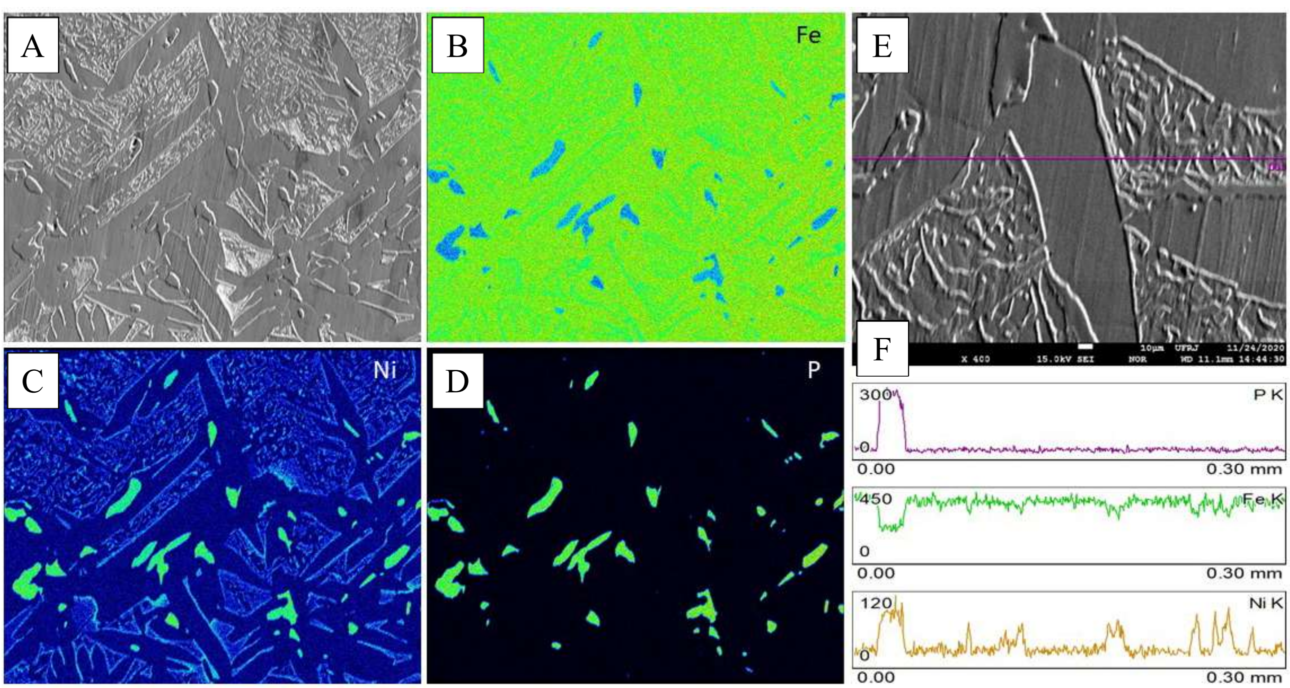

Figure 7 Cratheus iron meteorite prior to the MN/UFRJ fire, showing the reference, unaltered microstructure: A. SEM image of a plessitic Widmanstätten structure, with diverse plessite fields, taenite and kamacite lamellae. Phosphides (schreibersite) occur along several kamacite grains; B-D. SEM–EDS elemental distribution maps illustrating the sharp chemical delineation of schreibersite phosphide phases; E-F. Higher-magnification SEM image detailing the Widmanstätten pattern and associated plessitic regions. SEM–EDS line-scan showing the distribution of Ni and P along the indicated transect across phosphide and metallic phases.

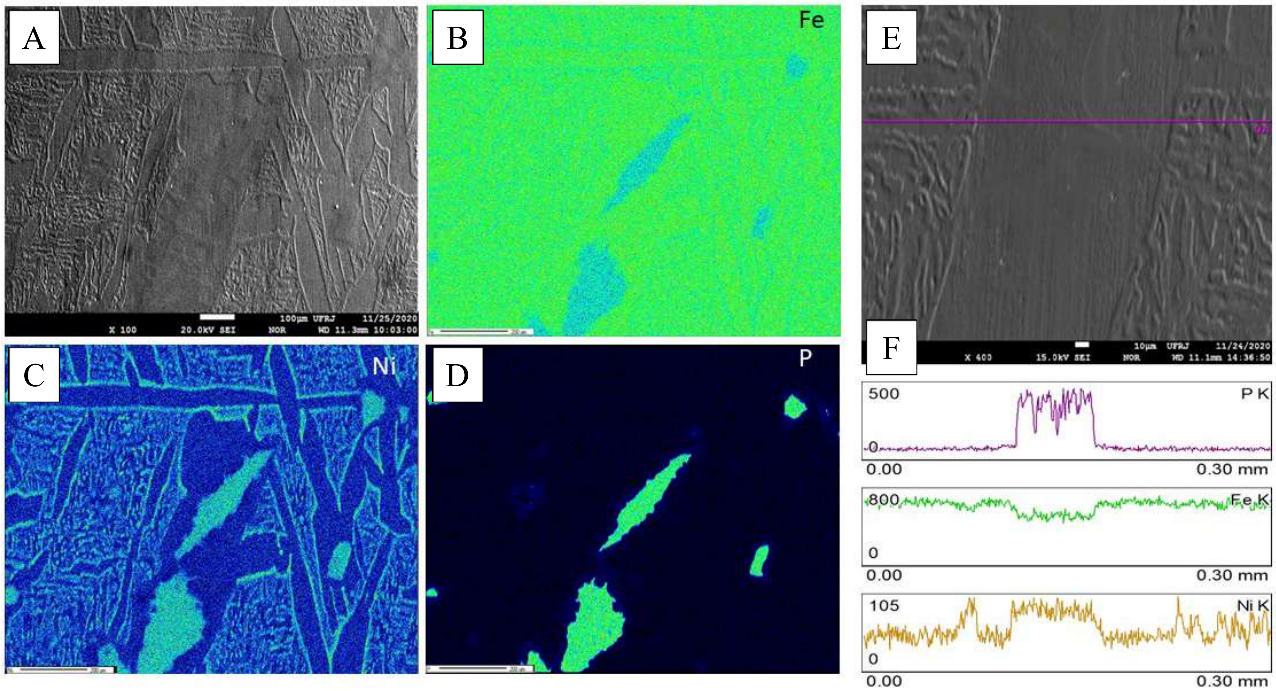

Figure 8 Cratheus iron meteorite after the MN/UFRJ fire, showing the effects of heating on the metallic microstructure: A. SEM image of a plessitic Widmanstätten structure with diverse plessite fields, taenite and kamacite lamellae. Phosphides (schreibersite) are strongly attenuated and locally almost indistinguishable along kamacite grains; B-D. SEM–EDS elemental distribution maps illustrating diffuse compositional boundaries of schreibersite phosphide phases, reflecting thermal alteration; E-F. SEM–EDS line-scan and elemental profiles of Ni and P across phosphide and adjacent metallic phases, showing that phosphides lose their angular outlines, become irregular or locally disappear, leaving only diffuse zones of phosphorus enrichment within kamacite as a result of annealing.

Table 5 Three principal levels of thermal damage were identified.

Thermal Damage Level	Fire Exposure Conditions	Observed Effects	Interpretive Significance
Level 0 No Thermal Damage	Areas not subjected to sustained or high-intensity heat flux (including the Bendegó exhibition sector and selected LABSONDA samples).	No detectable thermal alteration; Microstructures fully preserved.	Provides an essential pre-fire reference for reconstruction, comparison, and reclassification of thermally damaged meteorites.
Level 1 Minimal Thermal Damage	Exposure to low-intensity thermal fields and smoke without direct flame contact	Superficial soot deposition; Slight darkening; Absence of thermal metamorphism.	Alteration consistent with low temperature and/or short-duration exposure
Level 2 Moderate to Severe Thermal Damage	Heterogeneous high-temperature fields with episodes of direct flame contact, structural collapse, and prolonged heat retention	Mechanical fragmentation; Deposition of ash, molten materials, and corrosive particulates; Phase destabilization; Recrystallization; Partial to severe obliteration of primary microstructures.	Records complex thermal overprinting under extreme terrestrial fire conditions.

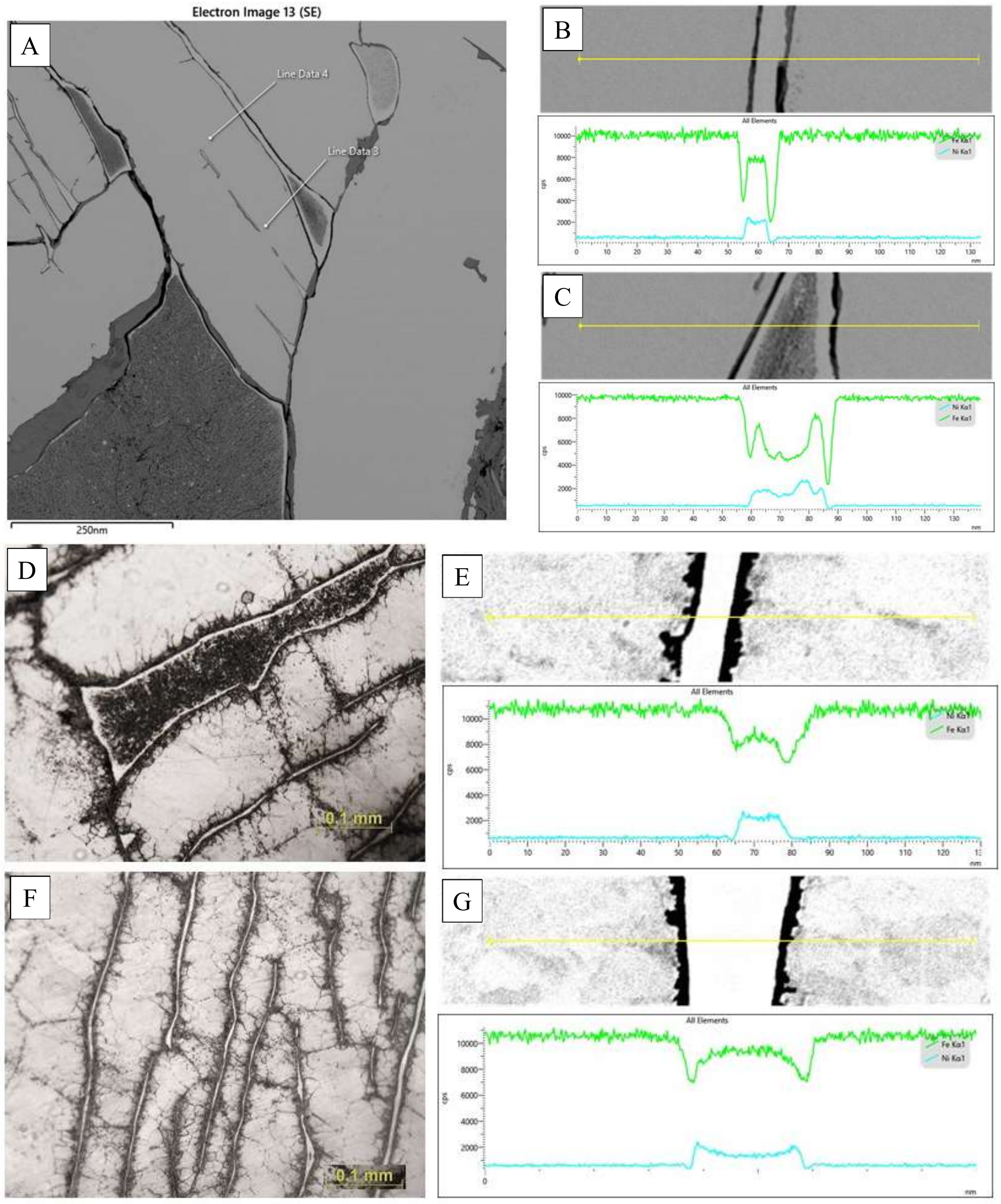

Figure 9 São João Nepomuceno (SJN) iron meteorite: A-C. SJN prior to the MN/UFRJ fire; A. Secondary electron (SE) image showing kamacite plates (light grey) and taenite laths, dark plessite fields, and oxide phases along grain boundaries (etched with 2% nital); B-C. Ni concentration profiles as a function of distance measured along the indicated transect across taenite, displaying two strongly asymmetric M-shaped profiles rather than the symmetric M-profiles typical of primary cooling. An unetched region corresponds to clear taenite, whereas the internal region corresponds to cloudy taenite finely decomposed into martensite (high-Ni plessite); C. In the central portion of the profile, the data show significant scatter, attributed to the martensitic plessite field; D-G. SJN after the MN/UFRJ fire; D. and F. Reflected-light microscopy images (etched with 2% nital) showing taenite, dark plessite and recrystallized kamacite lamellae. Localized darkening along kamacite grain boundaries adjacent to taenite reflects carbon redistribution induced by thermal exposure; E. and G. Ni concentration profiles as a function of distance measured along the indicated transect across taenite, showing the absence of the characteristic M-shaped profile.

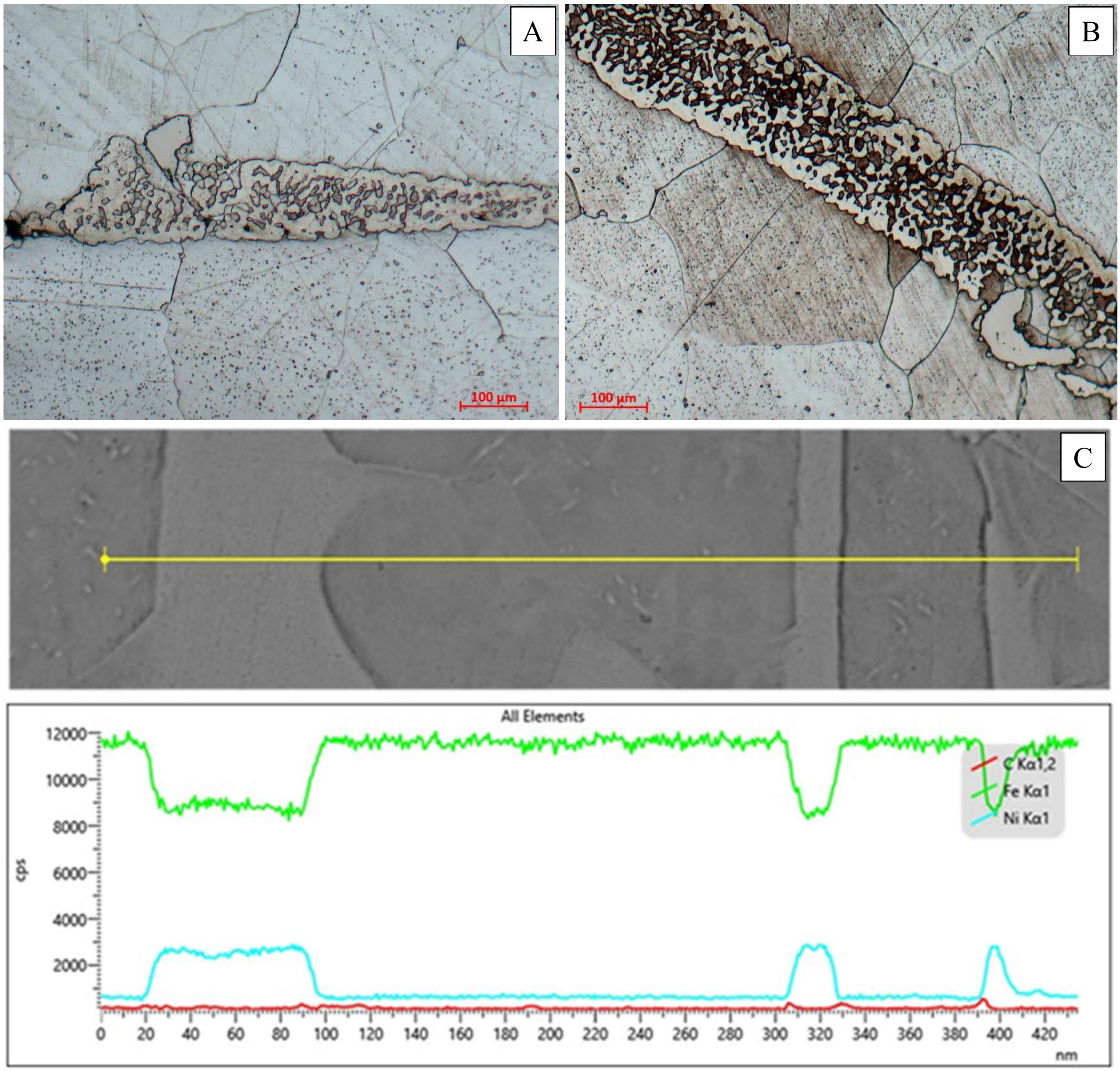

Figure 10 Microstructure of the Cratheus iron meteorite before and after the MN/UFRJ fire, illustrating the effects of reheating under reflected-light microscopy: A. Pre-fire microstructure showing a band of spheroidized taenite particles between two kamacite plates, together with fine taenite laths precipitated within kamacite. Neumann lines and subgrain structures in kamacite record the effects of cosmic shock and subsequent annealing in space; B. Post-fire microstructure displaying spheroidized taenite between two kamacite lamellae within recrystallized kamacite, indicating thermal overprinting; C. Ni concentration profile across Widmanstätten ferrite plates (α) and a taenite lamella (austenite, γ), showing the absence of the characteristic M-shaped Ni profile typically developed in taenite during primary cooling. This attenuation indicates that the original zoning was previously modified by thermal processing (e.g., space/cosmic heating) prior to the MN/UFRJ fire.

sequence of fire-related microstructural changes observed across the MN/UFRJ collection is synthesized in Table 6, which defines successive fire stages on the basis of diagnostic metallographic criteria and associated temperature ranges, thereby providing a standardized basis for interpretation, documentation, and comparison.

By integrating these observations with the experimentally and observationally constrained metallographic stability fields summarized in Table 4, the proposed classification establishes a direct correspondence between literature-derived thermal thresholds and the damage stages documented in the MN/UFRJ iron meteorites,

Table 6 Progressive stages of thermal alteration ("Fire stages") in iron meteorites.

Fire stage	Effects from sustained heating	Estimated Temp. (°C)
F0 Unheated	No thermal effects; Pristine Widmanstätten structure; Intact Neumann lines.	<300
F1 Very low heating	Early taenite diffusion; Blurring of Neumann lines; Microcracking; Initial plessite alteration; Recovery softening of kamacite and taenite.	300–550
F2 Low heating	Partial loss of Widmanstätten pattern; Taenite diffusion fronts; Kamacite recrystallization; Incipient schreibersite melting; Oxide-filled fractures.	550–700
F3 Moderate heating	Significant Widmanstätten degradation; Strong granulation; Taenite destabilization; Schreibersite melting.	700–900
F4 Strong heating	Octahedral structure discontinuous; Strong diffusion regime; Widespread taenite destabilization.	900–970
F5 Very strong heating	Widmanstätten nearly obliterated; Pervasive granulation; Phase homogenization; Immiscible Fe–Ni–P melts; Vesiculated metal.	970–1100
F6 Extreme heating	Partial Fe–Ni melting; Melt pool coalescence; Severe texture destruction.	1100–1300
F7 Fully melted	Complete metal melting; Fusion crust development; Resolidification from total melt.	>1300

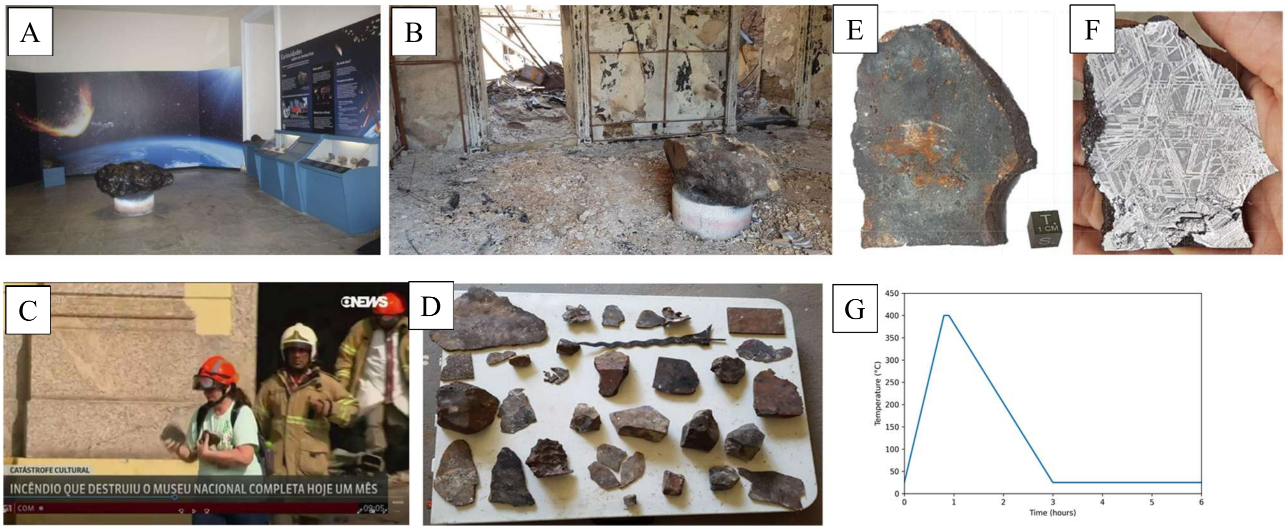

Figure 11 Documentation of the thermal conditions and preservation state of metallic meteorites at Level 1 of the MN/UFRJ during the 2018 fire, where negligible thermal alteration was observed: A. Exhibition Hall adjacent to the Bendegó meteorite, showing the display "From Genesis to Apocalypse" prior to the fire, where metallic meteorites were exposed; B. Same area on the morning following the fire, showing debris accumulation but absence of active combustion. The area was already cold at the time of access; C. Field documentation of the author during the recovery of meteorites from the debris on the morning after the fire, confirming that specimens were retrieved at ambient temperature; D. Meteorites recovered on the morning following the fire; E. Carlton iron meteorite as recovered from the ashes, showing superficial oxidation products; F. Polished and etched section of the Carlton meteorite after recovery, revealing a well-preserved Widmanstätten pattern, with no detectable microstructural modification attributable to heating; G. Schematic thermal profile inferred for Level 1, indicating moderate peak temperatures (≤ 400 °C) followed by rapid air cooling, consistent with the absence of diffusion-controlled microstructural changes.

anchoring the interpretative framework within a robust and well-established body of metallographic knowledge.

Given that relatively mild heating (~500 °C) is sufficient to modify Neumann bands, plessite fields, recrystallization textures, and taenite stability, this classification system extends beyond the assessment of recent fire-related damage. It also provides a systematic tool for recognizing and discriminating ancient anthropogenic reheating in historical meteorite collections, contributing to the critical reassessment of legacy specimens and enhancing the reliability of metallographic interpretations derived from museum-held materials.

6 Conclusion

Owing to the markedly different degrees of thermal exposure experienced by the iron meteorites within the MN/UFRJ collection, we developed a classification system defining progressive temperature-related damage stages from F0 to F7 (Table 6). This scale ranges from specimens that remain intact and show no evidence of reheating (F0) to those that were completely melted and subsequently resolidified (F7). The proposed scheme is intended to function as a standardized damage index for fire-affected meteorites and is being incorporated into the catalogue records and physical labels of each specimen curated in the Meteorite Sector of the MN/UFRJ.

All meteorites affected by the 2018 fire are being systematically examined and assigned a fire-damage code, providing a consistent framework for curatorial documentation and future scientific investigation. Specimens unaffected by heat, including those originally curated at LABSONDA/UFRJ, are being reincorporated into the MN/UFRJ catalogue through sequential registration aligned with the last salvaged inventory entry. In addition, all meteorites from the exhibition *From Genesis to Apocalypse* have been identified, stabilized, and restored, and are currently preserved and displayed in public exhibitions.

Beyond the specific case of the MN/UFRJ, the classification scheme presented here offers a transferable tool for assessing and documenting fire-related thermal damage in meteorite collections housed in museums worldwide. By explicitly accounting for terrestrial reheating and its metallographic consequences, this approach enhances both the scientific interpretation of iron meteorites and the long-term conservation of meteoritic heritage, reinforcing the role of metallographic analysis as a critical instrument in the preservation of cultural and scientific collections.

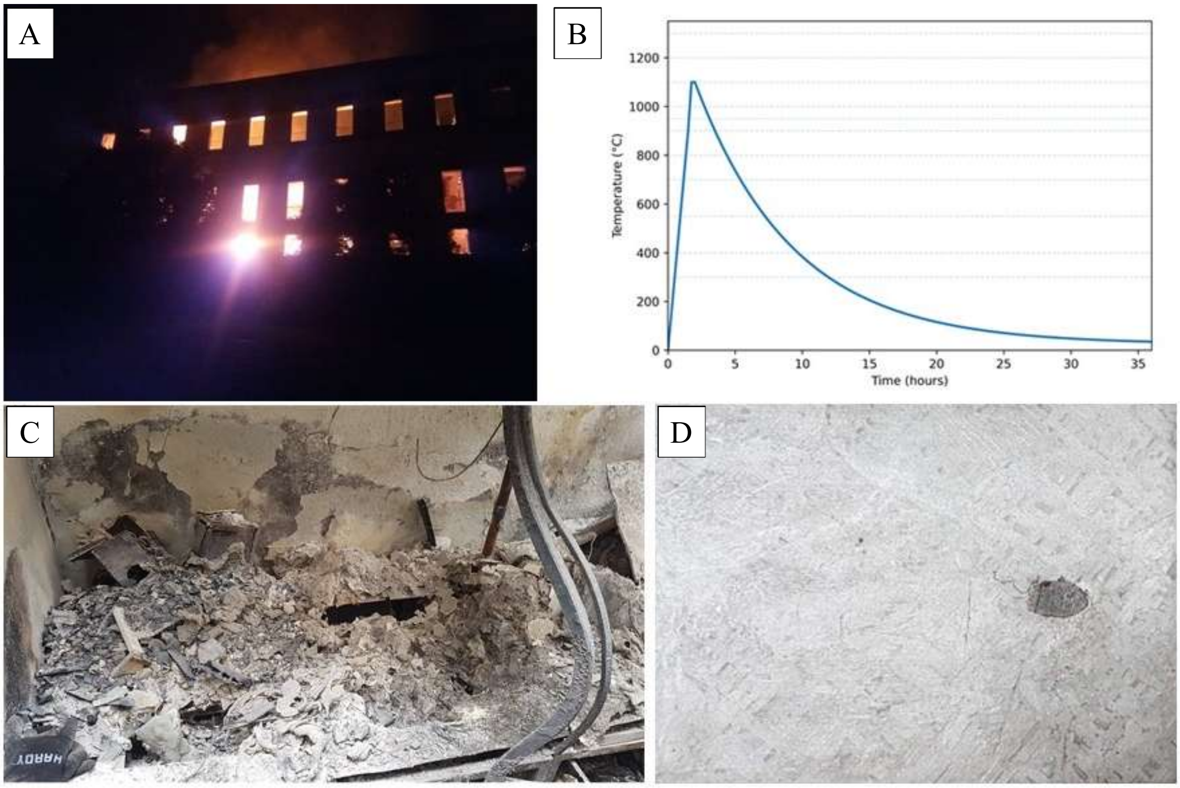

Figure 12 Documentation and interpretation of the high-temperature regime experienced in the rear sector of the MN/UFRJ during the 2018 fire (Level 2): A. View of the posterior area of the museum, where combustion persisted for several hours, supplying sustained heat to the collection storage sector; B. Schematic thermal profile inferred for this area, reproducing furnace-like conditions generated by prolonged heating and thermal insulation by collapsed structural elements, resulting in slow post-fire cooling; C. Metallic meteorites as found inside storage cabinets beneath debris, illustrating burial under rubble that acted as an insulating layer and promoted extended exposure to elevated temperatures; D. Cape York iron meteorite showing a dull Widmanstätten structure under reflected-light microscopy, indicative of diffusion-dominated thermal overprinting and loss of structural sharpness associated with prolonged reheating and slow cooling.

7 References

Axon, H.J. 1963, 'Destruction of the Widmanstätten structure in iron meteorites by laboratory heat treatment', *Nature*, vol. 197, pp. 1074–5, DOI: 10.1038/1971074a0

Berwerth, F. 1914, Die Meteoriten in Sammlungen und ihre Geschichte.

Bland, P.A. & Artemieva, N.A. 2006, 'The Rate of Small Impacts on Earth', *Meteoritics & Planetary Science*, vol. 41, pp. 607–31, DOI: 10.1111/j.1945-5100.2006.tb00485.x

Bryson, J.F.J., Nichols, C.I.O., Herrero-Albillos, J., Kronast, F., Kasama, T., Alimadadi, H., van der Laan, G., Nimmo, F. & Harrison, R.J. 2015, 'Long-lived magnetism from solidification-driven convection on the pallasite parent body', *Nature*, vol. 517, pp. 472–5, DOI: 10.1038/nature14114

Buchwald, V.F. 1975, *Handbook of Iron Meteorites: Their History, Distribution, Composition and Structure*, 3 vols, University of California Press, Berkeley.

Buseck, P.R. 1969, 'Phosphide from Meteorites: Barringerite, a New Iron-Nickel Mineral', *Science*, vol. 165, pp. 169–71, DOI: 10.1126/science.165.3889.169

Choi, B.G., Ouyang, X. & Wasson, J.T. 1995, 'Classification and origin of IAB and IIICD iron meteorites', *Geochimica et Cosmochimica Acta*, vol. 59, no. 3, pp. 593–612.

Clarke, R.S. & Scott, E.R. D. 1980, 'Ordering of FeNi in clear taenite from meteorites', *Nature*, vol. 287, p. 255, DOI: 10.1038/287255a0

Cohen, E. 1905, Meteoritenkunde, Schweizerbartsche Verlagshandlung, Stuttgart.

Goldberg, E., Uchiyama, A. & Brown, H. 1951, 'The distribution of nickel, cobalt, gallium, palladium and gold in iron meteorites', *Geochimica et Cosmochimica Acta*, vol. 2, no. 1, pp. 1–25.

Goldstein, J.I. & Michael, J.R. 2006, 'The Formation of the Widmanstätten Pattern in Meteorites', *Meteoritics & Planetary Science*, vol. 41, pp. 553–70, DOI: 10.1111/j.1945-5100.2006.tb00482.x

Goldstein, J.I. & Ogilvie, R.E. 1965, 'The growth of the Widmanstätten pattern in metallic meteorites', *Geochimica et Cosmochimica Acta*, vol. 29, pp. 893–920.

Goldstein, J.I., Scott, E.R.D. & Chabot, N.L. 2009, 'Iron meteorites: Crystallization, thermal history, parent bodies, and origin', *Chemie der Erde*, vol. 69, pp. 293–325, DOI: 10.1016/j.chemer.2009.01.002

Goldstein, J.I., Scott, E.R.D. & Yang, J. 2009, 'Metallographic Cooling Rates of Iron Meteorites: Assessment and Refinement', *Chemie der Erde*, vol. 69, pp. 293–303.

Goldstein, J.I. & Short, J.M. 1967, 'Cooling rates of iron meteorites—determined from taenite–kamacite profiles', *Geochimica et Cosmochimica Acta*, vol. 31, pp. 1733–70.

Hutchison, R. 2004, *Meteorites: A Petrologic, Chemical and Isotopic Synthesis*, Cambridge Planetary Science Series, Cambridge.

Kase, T. 1925, 'Thermal alteration in iron meteorites', *Science Reports of the Tohoku Imperial University*, vol. 14, pp. 173–217.

Kracher, A., Willis, J. & Wasson, J.T. 1980, 'Chemical classification of iron meteorites-IX. A new group (IIF), revision of IAB and IIICD, and data on 57 additional irons', *Geochimica et Cosmochimica Acta*, vol. 44, pp. 773–87.

Langenhorst, F. 2002, 'Shock Metamorphism of Some Minerals: Basic Introduction and Microstructural Observations', *Bulletin of the Czech Geological Survey*, vol. 77, no. 4, pp. 265–82.

Lovering, J.F., Nichiporuk, W., Chodos, A. & Brown, H. 1957, 'The distribution of gallium, germanium, cobalt, chromium, and copper in iron and stony-iron meteorites in relation to nickel content and structure', *Geochimica et Cosmochimica Acta*, vol. 11, pp. 263–78.

Malvin, D.J., Wang, D. & Wasson, J.T. 1984, 'Chemical classification of iron meteorites - X. Multielement studies of 43 irons, resolution of group IIIE from IIIAB, and evaluation of Cu as a taxonomic parameter', *Geochimica et Cosmochimica Acta*, vol. 48, no. 4, pp. 785–804.

Massalski, T.B., Subramanian, P.R., Okamoto, H. & Kacprazak, L. 1990, Binary Alloy Phase Diagrams, 2nd edn, ASM International, Materials Park.

Monteiro, F.A. 2018, 'Caracterização Histórica, Mineralógica e Metalográfica de Artefatos Forjados Supostamente Utilizando Ferro Meteorítico', Master dissertation, Universidade Federal do Rio de Janeiro, Rio de Janeiro.

Monteiro, F.A., Oliveira, F.A., Tosi, A.A. & Zucolotto, M.E. 2020, 'Recognition and Characterization of Metal Meteorites Rescued After Fire of the National Museum/UFRJ', Proceedings of XLIII Reunião Anual da SAB, vol. 32, no. 1, pp. 167–8.

Norton, O.R. & Chitwood, L. 2008, Field Guide to Meteors and Meteorites.

Perry, S.H. 1944, The Metallography of Meteoric Iron, U.S. National Museum Bulletin 184.

Ramdohr, P. 1967, 'On the wide-spread paragenesis of ore minerals originating during serpentinization', *Geologiya Rudnykh Mestorozhdenii*, vol. 2, pp. 32–43.

Reed, S.J.B. 1965, 'Characteristic fluorescence corrections in electron-probe microanalysis', *British Journal of Applied Physics*, vol. 16, no. 7, p. 913.

Reisener, R.J. & Goldstein, J.I. 2003, 'Ordinary chondrite metallography: Part 1. Fe-Ni taenite cooling experiments', *Meteoritics & Planetary Science*, vol. 38, pp. 1669–78.

Rose, G. 1864, 'Ueber das Verhältniss der Krystallformen des Systems vom regulären Oktaeder zu den Krystallformen des Systems vom regulären Hexaëder', *Poggendorffs Annalen der Physik und Chemie*, vol. 123, no. 2, pp. 481–511.

Ruzicka, A., Grossman, J.N., Garvie, L. & Benedix, G.K. 2014, 'The Meteoritical Bulletin, No. 100', *Meteoritics & Planetary Science*, vol. 49, pp. E1–E101.

Ruzicka, A. & Hutson, M. 2010, 'Comparative petrology of silicates in the Udei Station (IAB) and Miles (IIE) iron meteorites: Implications for the origin of silicate-bearing iron', *Geochimica et Cosmochimica Acta*, vol. 74, no. 2, pp. 394–433.

Scott, E.R.D. & Wasson, J.T. 1975, 'Classification and properties of iron-meteorites', *Reviews of Geophysics*, vol. 13, pp. 527–46.

Scott, E.R.D. & Wasson, J.T. 1976, 'Chemical classification of iron meteorites. VIII - Groups IC, IIE, IIIF and 97 other irons', *Geochimica et Cosmochimica Acta*, vol. 40, pp. 103–15.

Sorby, H.C. 1887, 'On The Microscopical Structure of Iron and Steel', *J Iron Steel Inst*, vol. 1, pp. 255–88.

Vogel, R. 1927, 'Über die Strukturformen des Meteoreisens und Ihre Spezielle Beeinflussung durch Umwendlung und Beigemengten Phosphor', *Abhandlunger der Gesellschaft der Wissenschaften zu Göttingen, Mathematisch-physikalische Klasse*, vol. 12, no. 2.

Vogel, R. 1932, 'Eine umfassendere Deutung der Gefugeerscheinungen des Meteoreisens durch das Zustandsdiagramm des ternaren Systems Eisen-Nickel-Phosphor', *Abhandlungen der Gesellschaft der Wissenschaften zu Gottingen, Mathematisch-physikalische Klasse*, vol. 3, no. 6.

Walker, R.J., McDonough, W.F., Honesto, J., Chabot, N.L., McCoy, T.J., Ash, R.D. & Bellucci, J.J. 2008, 'Modeling fractional crystallization of group IVB iron meteorites', *Geochimica et Cosmochimica Acta*, vol. 72, no. 8, pp. 2198–216.

Wasson, J.T. 1967, 'The chemical classification of iron meteorites: I. A study of iron meteorites with low concentrations of gallium and germanium', *Geochimica et Cosmochimica Acta*, vol. 31, no. 2, pp. 161–80.

Wasson, J.T. & Kimbeblin, J. 1967, 'The chemical classification of iron meteorites—II. Irons and pallasites with germanium concentrations between 8 and 100 ppm', *Geochimica et Cosmochimica Acta*, vol. 31, no. 10, pp. 2065–93.

Wasson, J.T. 1969, 'The chemical classification of iron meteorites—III. Hexahedrites and other irons with germanium concentrations between 80 and 200 ppm', *Geochimica et Cosmochimica Acta*, vol. 33, no. 7, pp. 859–68.

Wasson, J.T. 1974, Meteorites: Classification and Properties, Springer, New York.

Wasson, J.T. & Wang, J. 1986, 'A nonmagmatic origin of group-IIE iron meteorites', *Geochimica et Cosmochimica Acta*, vol. 50, no. 5, pp. 725–32.

Wasson, J.T. 1990, 'Ungrouped Iron Meteorites in Antarctica: Origin of Anomalously High Abundance', *Science*, vol. 249, no. 4971, pp. 900–2.

Wasson, J.T. 1999, 'Trapped melt in IIIAB irons; solid/liquid elemental partitioning during the fractionation of the IIIAB magma', *Geochimica et Cosmochimica Acta*, vol. 63, no. 18, pp. 2875–89.

Wasson, J.T. & Richardson, J.W. 2001, 'Fractionation trends among IVA iron meteorites: Contrasts with IIIAB trends', *Geochimica et Cosmochimica Acta*, vol. 65, no. 6, pp. 951–70.

Wasson, J.T. & Kallemeyn, G.W. 2002, 'Classification and compositional framework of iron meteorites', *Geochimica et Cosmochimica Acta*, vol. 66, pp. 2445–73.

Wasson, J.T. & Huber, H. 2006, 'Compositional trends among IID irons; their possible formation from the P-rich lower magma in a two-layer core', *Geochimica et Cosmochimica Acta*, vol. 70, no. 24, pp. 6153–67.

Wasson, J.T., Huber, H. & Malvin, D.J. 2007, 'Formation of IIAB iron meteorites', *Geochimica et Cosmochimica Acta*, vol. 71, no. 3, pp. 760–81.

Willis, J. & Goldstein, J.I. 1981, 'Solidification zoning and metallographic cooling rates of chondrites', *Nature*, vol. 293, pp. 126–7.

Wood, J.A. 1964, 'The cooling rates and parent planets of several iron meteorites', *Icarus*, vol. 3, pp. 429–59.

Wood, J.A. 1968, Meteorites and the Origin of Planets, Earth and Planetary Science Series, McGraw-Hill Book Co., New York.

Yang, C.W., Williams, D.B. & Goldstein, J.I. 1996, 'A new empirical cooling rate indicator for iron meteorites', *Geochimica et Cosmochimica Acta*, vol. 60, pp. 263–72.

Yang, J. & Goldstein, J.I. 2005, 'The formation of the Widmanstätten structure in meteorites', *Meteoritics & Planetary Science*, vol. 40, no. 2, pp. 239–53.

Yang, J., Goldstein, J.I. & Scott, E.R.D. 2007, 'Iron Meteorite Cooling Rates: New Constraints from the Ni Concentration Profiles in Plessite', *Geochimica et Cosmochimica Acta*, vol. 71, pp. 4087–101.

Yang, J., Goldstein, J.I. & Scott, E.R.D. 2010, 'Main-Group Pallasites: Chemical Compositions, Cooling Rates, and Origin', *Geochimica et Cosmochimica Acta*, vol. 74, pp. 4471–92.

Yang, J., Goldstein, J.I., Michael, J.R., Kotula, P.G. & Scott, E.R.D. 2010, 'Thermal history and origin of the IVB iron meteorites and their parent body', *Geochimica et Cosmochimica Acta*, vol. 74, pp. 4493–506.

Zucolotto, M.E., Fonseca, A.C., Antonello, L.L. & Monteiro, F.A. 2013, Decifrando os Meteoritos, Editora da Universidade Federal do Rio de Janeiro – Museu Nacional, Rio de Janeiro.

Zucolotto, M.E., Ornellas, I.D. & Tosi, A.A. 2022, 'Using HHXRF to Screen Rescued Meteorites from the National Museum's Fire', Proceedings of 85th Annual Meeting of The Meteoritical Society, vol. 85, no. 2695.

Zucolotto, M.E., Tosi, A.A. & Monteiro, F.A. 2019, viewed 8 Dec. 2025, http://www.meteorite-times.com/the-fire-of-the-national-museum-of-rio-de-janeiro.

Author contributions

Felipe Abrahão Monteiro: conceptualization; data curation; formal analysis; validation; visualization; writing – original draft; writing – review & editing. **Maria Elizabeth Zucolotto:** conceptualization; data curation; formal analysis; investigation; methodology; supervision; validation; writing – original draft. **Amanda Araujo Tosi:** data curation; formal analysis; investigation; software.

Conflict of interest

The authors declare no conflict of interest.

Data availability statement

All data included in this study are publicly available in the literature.

Funding information

Not applicable.

How to cite:

Monteiro, F.A., Zucolotto, M.E. & Tosi, A.A. 2026, 'Fire-Induced Thermal Alteration in Iron Meteorites: Metallographic Analysis of the 2018 Disaster at the National Museum of Rio de Janeiro', *Anuário do Instituto de Geociências,* 49:e71839. https://doi.org/10.11137/1982-3908_2026_49_71839